

2021

Discharge Mode Transition in He/Ar Atmospheric Pressure Plasma Jet and its Inactivation Effect Against Tumor Cells *In Vitro*

Bolun Pang

Zhijie Liu


Sitao Wang

Yuting Gao

Huaiyan Zhang

See next page for additional authors

Follow this and additional works at: https://digitalcommons.odu.edu/bioelectrics_pubs

 Part of the [Biomedical Engineering and Bioengineering Commons](#), [Nanoscience and Nanotechnology Commons](#), and the [Organic Chemistry Commons](#)

Original Publication Citation

Pang, B., Liu, Z., Wang, S., Gao, Y., Zhang, H., Zhang, F., Tantai, X., Xu, D., Liu, D., & Kong, M. G. (2021). Discharge mode transition in a He/Ar atmospheric pressure plasma jet and its inactivation effect against tumor cells *in vitro*. *Journal of Applied Physics*, 130(15), 1-12, Article 153301. <https://doi.org/10.1063/5.0063135>

This Article is brought to you for free and open access by the Frank Reidy Research Center for Bioelectrics at ODU Digital Commons. It has been accepted for inclusion in Bioelectrics Publications by an authorized administrator of ODU Digital Commons. For more information, please contact digitalcommons@odu.edu.

Authors

Bolun Pang, Zhijie Liu, Sitao Wang, Yuting Gao, Huaiyan Zhang, Feng Zhang, Xiamin Tantai, Dehui Xu, Dingxin Liu, and Michael G. Kong

Discharge mode transition in a He/Ar atmospheric pressure plasma jet and its inactivation effect against tumor cells *in vitro*

Cite as: J. Appl. Phys. **130**, 153301 (2021); doi: [10.1063/5.0063135](https://doi.org/10.1063/5.0063135)

Submitted: 12 July 2021 · Accepted: 30 September 2021 ·

Published Online: 15 October 2021



Bolun Pang,¹ Zhijie Liu,^{1,a)} Sitao Wang,¹ Yuting Gao,¹ Huaiyan Zhang,¹ Feng Zhang,¹ Xiamin Tantai,¹ Dehui Xu,¹ Dingxin Liu,¹ and Michael G. Kong^{1,2,3,a)}

AFFILIATIONS

¹State Key Laboratory of Electrical Insulation and Power Equipment, Centre for Plasma Biomedicine, School of Electrical Engineering, Xi'an Jiaotong University, Xi'an, Shaanxi 710049, People's Republic of China

²Frank Reidy Center for Bioelectronics, Old Dominion University, Norfolk, Virginia 23508, USA

³Department of Electrical and Computer Engineering, Old Dominion University, Norfolk, Virginia 23529, USA

^{a)}Authors to whom correspondence should be addressed: liuzhijie2010@163.com and mglin5g@gmail.com

ABSTRACT

Discharge characteristic comparisons between He and Ar plasma jets have been extensively reported, but is rarely reported for the comprehensive study of discharge mode transition from He jet to Ar jet, especially its induced liquid chemistry and biological effect. In this paper, we investigate the plasma jet mode transformation by varying the Ar contents in the He/Ar mixing working gas, particularly focusing on the effect of liquid chemistry of plasma activated water (PAW) and the corresponding inactivation effect against tumor cells *in vitro*. The mode transition process from He jet to Ar jet is characterized by the discharge images, the spatial temporal evolution, and the electrical and spectra measurements. It is found that the plasma jet mode displays a transition from diffuse to filamentous mode, which significantly affects the gaseous reactive species production and the ability to deliver into liquid, resulting in a huge difference in physicochemical properties and the concentration of reactive oxygen and nitrogen species in PAW. Furthermore, the A549 lung cancer cell is utilized to reveal the inactivation effect against tumor cells induced by PAW during discharge mode transition, and it is found that the PAW induced by Ar plasma jet can lead to the higher apoptosis efficiency of cancer cells due to the high production of key species (NO_2^- , H_2O_2 , and $\text{ONOO}^-/\text{ONOOH}$) under filamentous mode. This study would provide deep insights into the nature of liquid physicochemistry and its anticancer effect during plasma jet mode transformation.

Published under an exclusive license by AIP Publishing. <https://doi.org/10.1063/5.0063135>

I. INTRODUCTION

Atmospheric pressure plasma jet (APPJ) as a promising generator of cold temperature plasma has been rapidly developed in recent decades and processes outstanding effects in nanotechnology,^{1,2} organic chemistry,^{3,4} and biomedicine.^{5–7} APPJ can be ignited in the atmospheric environment and then contact with the liquid which efficiently delivers the chemical reactive oxygen and nitrogen species (RONS: ROS and RNS) into the treated target. Helium (He) and Argon (Ar), as commonly noble working gases used in plasma generation, have a huge difference in discharge characteristics.^{7–12} Many studies about the difference between He jet and Ar jet have been researched. The main reason is due to

their different atomic structures and ionization potential. On the one hand, He has a higher ionization potential (24.6 eV) compared to Ar (15.8 eV), direct ionization is formed easier in Ar than in He due to the lower ionization energy, and the resistance of the ionized channel is small in Ar plasma, which will result in the Ar plasma jet being filamentary discharge.¹³ On the other hand, different ionization potentials lead to different capacities for Penning ionization.^{14,15} The He plasma jet belongs to diffuse mode which is characterized by the uniform current and homogeneous plasma distribution, and the plasma temperature is close to room temperature.¹⁶ Ar plasma jet belongs to filamentous mode and composed of discharge filaments with a short existence time, which leads to

the plasma distribution being more dispersed and the temperature of the plasma is higher than He, so the effect is less ideal than that of plasma with diffuse discharge.^{8,17} Wang *et al.* found that under the same working conditions, such as oxygen consumption, input power, and gas flow rate, Ar plasma jet has better energy transfer efficiency than He plasma jet.¹⁸ Chen *et al.* reported that the ionization energy and excitation energy of Ar were lower than that of He, and the influence of Ar gas flow was greater than that of He. These reasons can be used to explain the different characteristic plume morphology of He and Ar plasma in the open air.¹⁹ Ogawa *et al.* studied the aqueous species after the treatment of solution by He and Ar plasma and found that the production efficiency of He and Ar plasma jet for H_2O_2 and NO_3^- is different, while the production efficiency of NO_2^- is similar.²⁰ Although some attention has been carried out, the different dynamic behaviors of the plasma jets when He or Ar is a working gas alone are rarely comprehensively studied for the discharge mode transition from the He jet to the Ar jet, especially their induced liquid chemistry and biological effects, which motivated us to carry out the research in this paper. This research can effectively fill the knowledge gaps of the correlation between the jet mode transition and the biological effect.

In this work, we focus on the plasma jet mode transition by changing the Ar content in the He/Ar mixing working gas, especially on the effect of liquid chemistry of PAW and the corresponding

inactivation effect against tumor cells *in vitro* during mode transition. The mode transformation process is characterized by the discharge images, electrical measurements, spectra measurements, and spatial-temporal evolution. Furthermore, the A549 lung cancer cell is utilized to reveal the inactivation effect of PAW during the plasma jet mode transition process.

II. EXPERIMENTAL SETUP AND METHODS

A. Experimental setup

The schematic diagram of the experimental device in this study is shown in Fig. 1. The plasma jet was generated between a tungsten rod (high voltage) and copper foil on the outer wall of a quartz tube (grounded electrode). The high-voltage electrode was a tungsten rod with a length of 9 cm and a diameter of 1 mm. The dielectric was a cylindrical quartz tube with a 6 mm outer diameter and a 4 mm inner diameter. The voltage applied in the rod electrode was obtained by a voltage probe (Tektronix, P6015A), and the current through the ground electrode was obtained by a current monitor (Pearson, 2877). The oscilloscope (Tektronix, MDO3054) was used to record the pulsed voltage and current waveform. The parameters of pulse voltage, frequency, and widths were kept at 8 kV, 4 kHz, and 1 μs by a homemade high-voltage pulse power supply. The distance from the tube nozzle to the de-ionized water

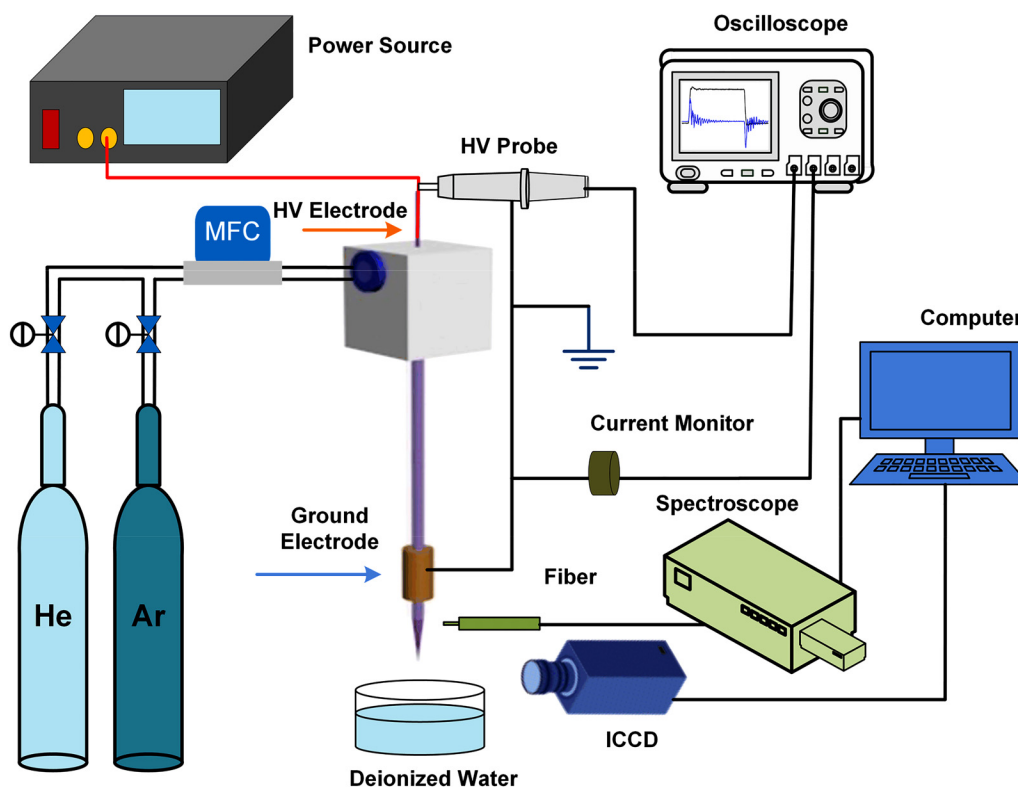


FIG. 1. Schematic diagram of the experimental system.

surface (liquid volume was 5 ml) was 20 mm. The high purity (5N) helium (He) and argon (Ar) were controlled by the mass flow controller (Sevenstar, CS200) into the plasma chamber from the gas inlet at a total rate of 3 SLM (standard liter per minute). The flow rate range of the mass flow controller was from 0.15 to 10 SLM. The additive Ar content in the 3 SLM working gas was 0, 0.25, 0.5, 1, 1.5, 2, and 3 SLM. The 0 SLM Ar addition means pure He and 3 SLM Ar means pure Ar.

B. Measurement methods

The APPJ plume images were captured by a digital camera (Nikon D7000) with an exposure time of 1.0 s. The spatial-temporal evolution processes of the plasma jet were recorded by an ICCD (Princeton Instruments, PI-Max3) with an exposure time of 10 ns and accumulation of 1000. The optical emission spectrum (OES) emitted by the reactive species in the plume was detected by an Andor SR-750i grating monochromator (grating grooving 1200 lines mm^{-1}) and an affiliated Andor iStar-DH334T intensified CCD camera. The OES measurement was carried out at the nozzle of the tube. The pH and conductivity of PAW were obtained by a pH meter (METTLER-TOLEDO, FE20) and conductivity meter (REX, DDS-307A), respectively. For long-lived species in the PAW, a microplate reader (Thermo Scientific Varioskan® Flash Reader) was employed with the Hydrogen Peroxide Assay Kit (Beyotime, S0038) and Griess reagent (Beyotime, S0021) to measure concentrations of H_2O_2 and NO_2^- . For the short-lived species, an electron spin resonance spectrometer (BrukerBioSpin GmbH, EMX) was used for detection. It should be noted that TEMPONE-H (1-Hydroxy-2,2,6,6-tetramethyl-4-oxo-piperidine, Enzo) with a concentration of 10 mM was used to trap O_2^- and peroxyxynitrite ($\text{ONOO}^-/\text{ONOOH}$), as these species would react with TEMPONE-H and produce the same product TEMPONE. So the concentration of TEMPONE represents the total concentration of both O_2^- and $\text{ONOO}^-/\text{ONOOH}$. The UV-visible spectrophotometer (Shimadzu, U-1800) was employed to detect the UV absorption profile of PAW with a standard optical path of 10 mm. The total

absorbance (range from 190 to 300 nm) was used to assess RONS delivery through the plasma jet to the liquid phase. The definition of total absorbance was calculated as²¹

$$\text{Total absorbance} \approx \int_{190}^{300} \text{Abs}(\lambda) d\lambda. \quad (1)$$

C. Cell apoptosis measurement

In this experiment, A549 lung cancer cells (American Type Culture Collection) were cultured in RoswellPark Memorial Institute (RPMI) 1640 medium, with 10% fetal calf serum, 1% (v/v) streptomycin, and penicillin. A total of 5000 cells were cultured on 96-well plates, meanwhile 20 000 cells on 24-well plates for 24 h to ensure cell adherence and stability, then refreshed with 50% RPMP1640 medium + 50% PAW for another 24 h. These plates were maintained in a humidified atmosphere of 5% CO_2 at 37 °C. After treatment, the relative cell viability was measured with a CellTiter-LumiTM luminescent cell viability assay kit (Beyotime, C0065S) by a Varioskan Flash microplate reader following the manuals provided by the manufacturer. In addition, to further explore the apoptosis situation, the treated cancer cells were stained with Annexin V-fluorescein isothiocyanate (Annexin V-FITC)/propidium iodide (PI) for 15 min in the dark and analyzed by flow cytometry (Accuri C6, BD Biosciences). All experimental data were presented as the mean \pm standard deviation (SD) and were analyzed by Student's *t* test. $p < 0.05$ was considered to indicate statistical significance (* $p < 0.05$, ** $p < 0.01$).

III. RESULTS AND DISCUSSION

A. Electrical and optical characteristics

Figure 2 shows the digital images of the plasma jet and the corresponding plume length during the conversion from pure He to pure Ar discharge. Compared with the pink color of the He jet, the red color fades considerably with the addition of a small amount of Ar (0.25 SLM), and the jet length increases slightly from

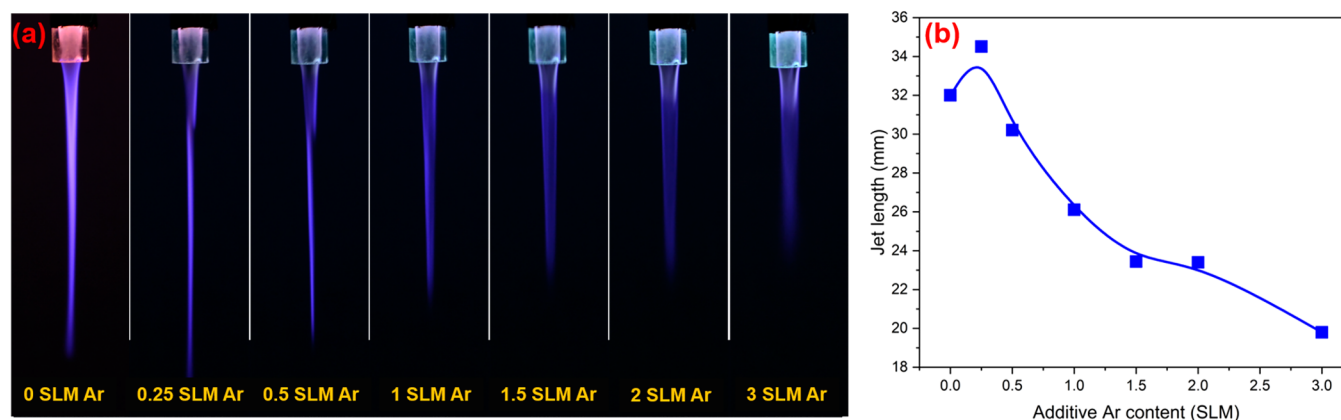


FIG. 2. (a) The discharge images and (b) plasma jet length during mode transition under different Ar addition in the working gas.

32.0 to 34.5 mm. The reason may be that the space electric field in the discharge area is enhanced by the small amount of Ar, and the propagation ability of charged particles is enhanced by the stronger electric field. With the further increase in Ar content from 0.25 to 3 SLM, the red gradually disappears and turns into white, and the jet length begins to shrink until reaches a minimum length of 19.8 mm for the pure Ar jet. From the perspective of discharge color and jet length, it is indicated that the mode transformation of the APPJ has occurred from a diffuse mode to a filamentary mode with Ar addition, but the evidence about mode transformation is confirmed by the ICCD images below.

Figure 3(a) shows the waveforms of voltage and total current for pure He and Ar plasma jets, respectively. The total current is generated at the rising and falling edge of voltage, and the current peak is higher under Ar working gas. When it comes to power, the discharge power of APPJ is obtained by integrating the product of the pulse voltage and total current,²²

$$P = f \int_0^T v(t)i(t)dt, \quad (2)$$

where f is the pulse frequency, T is the pulse period, $v(t)$ is the pulse voltage, and $i(t)$ is the total current. In this study, $f = 4$ kHz and $T = 1/f = 250 \mu\text{s}$. Figure 3(b) shows the effect of the additive Ar content in the working gas on power. The power decreases at first and then increases with Ar content. The inflection point of the curve is located at 1 SLM Ar addition, so this content may be the critical concentration for the discharge mode transition. Meanwhile, the discharge power of He/Ar mixed gas is lower than that of pure He and Ar. It can be seen that the discharge power of pure Ar plasma is higher than that of pure He, which is consistent with studies reported by Lee *et al.*²³

The spatial-temporal resolved images characterizing the behavior of plasma plume propagating during transition are shown in Fig. 4 under the same experimental conditions as in Fig. 2. As can be seen, a bright plasma bullet is generated at the rising edge of the pulse voltage. In pure He discharge, the plasma bullet shows a similar shape to the droplet. After Ar doping, the front segment gradually becomes smaller, and the bullet head transforms from a similar shape to a spindle. With Ar is introduced into the working gas, the seed electrons that originate from the ionization of Ar atoms may direct the annular discharge toward the flow axis, and in pure He, photoionization can only occur along with the core gas-air interface, resulting in an annular discharge.²⁴ So the shape of the plasma head changes. With time going by, the plasma bullet rapidly grows to its largest and brightest, then gradually shrinks and darkens as it travels through the air, eventually vanishing. At the same time, the discharge channel brightened obviously at the rising edge ($0.13 \mu\text{s}$) and falling edge ($1.03 \mu\text{s}$) of the pulse owing to the current peak generating the voltage. Under different additive Ar contents, it can be seen that the time of the plasma bullet finally dissipated is different and the maximum distance to travel is different. Taken together, these results suggest that the discharge mode transforms from diffuse mode to filamentous mode with the increase in Ar content in the working gas.

In order to explore the propagation of plasma jet in the open air during plasma jet mode transformation, Fig. 5 shows the evolution of bullet velocity with time under four conditions of working gas, which are 0 SLM Ar, 0.25 SLM Ar, 1 SLM Ar, and 3 SLM Ar. It can be seen that the plasma velocity increases sharply, then gradually slow down to 0, indicating plasma dissipates. As for the maximum velocity, the velocity of 0.25 SLM Ar plasma reaches approximately 4.10×10^4 m/s, followed by 0 SLM and 1 SLM Ar APPJ with 3.26×10^4 and 3.24×10^4 m/s, while 3 SLM Ar exhibits

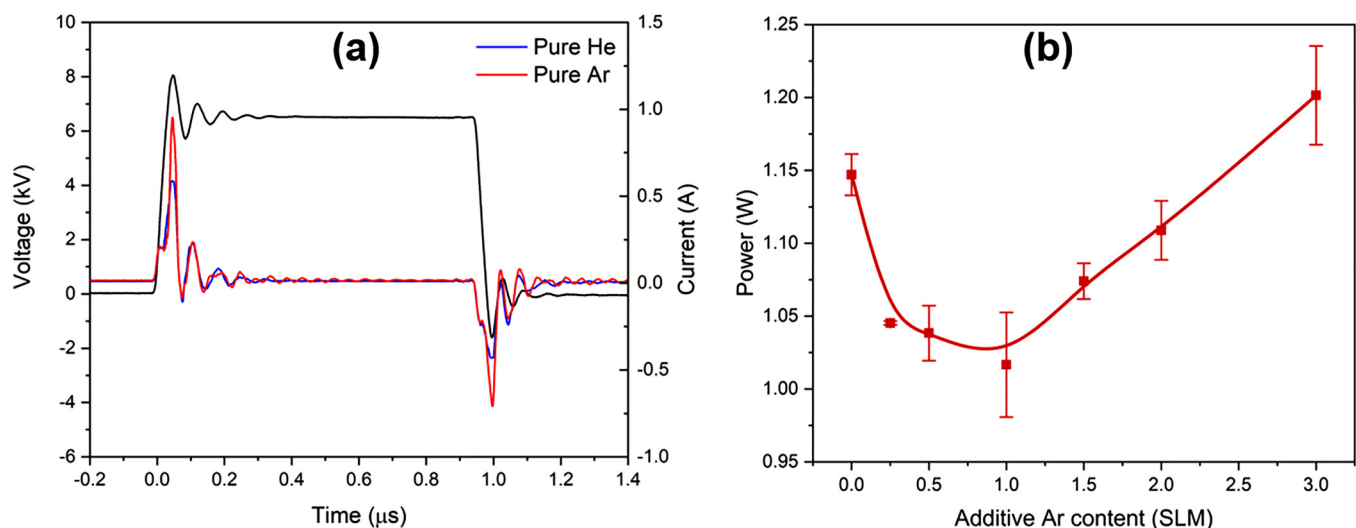


FIG. 3. (a) Typical waveforms of voltage and total current for pure He and Ar plasma jet, respectively. (b) The effect of the additive Ar content in the working gas on the discharge power.

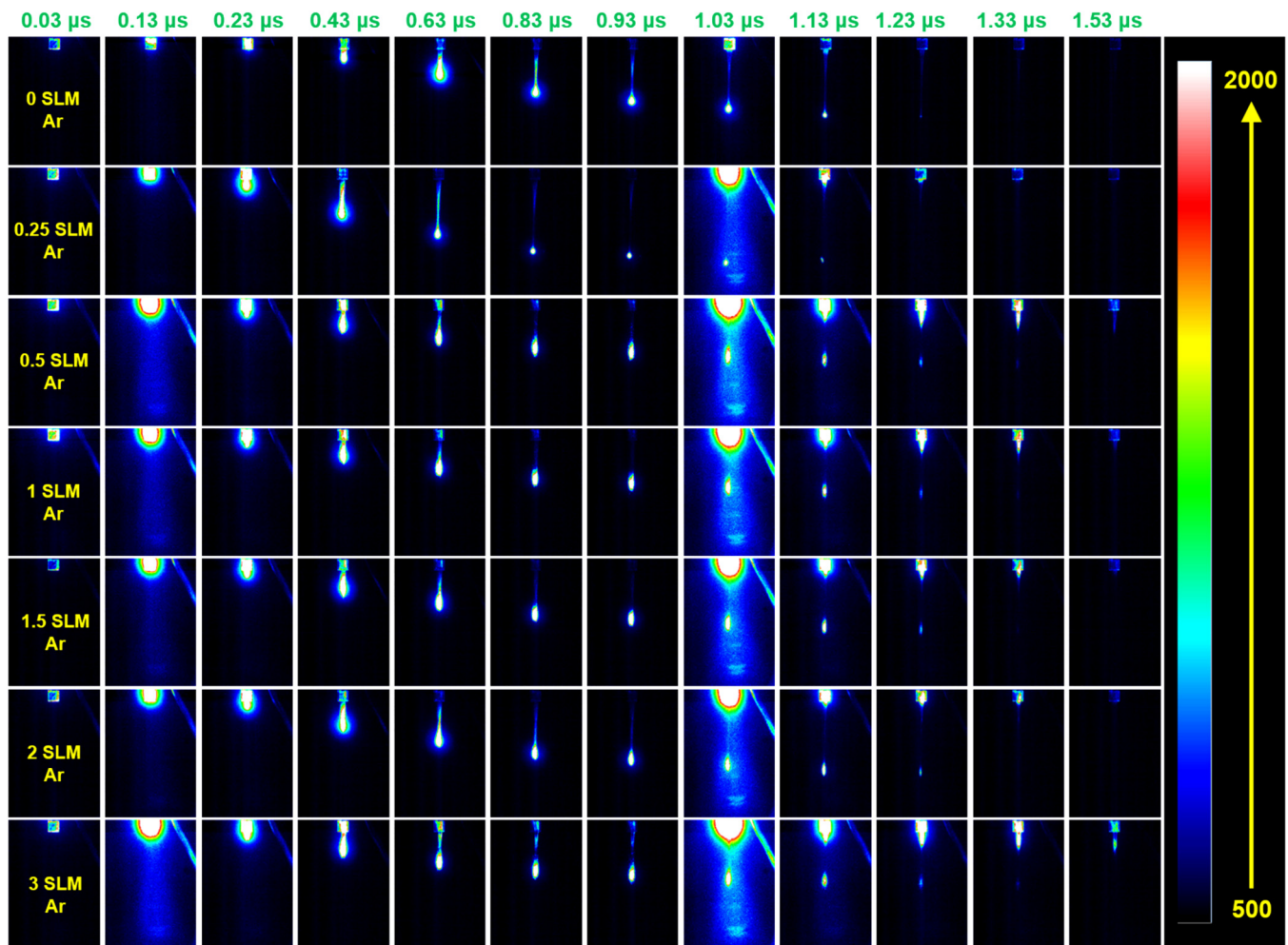


FIG. 4. The spatial-temporal resolved images of plasma jets in one pulsed period under different Ar addition in the working gas.

the lowest propagating velocity about 2.6×10^4 m/s. In the process of acceleration, it takes approximately $0.45 \mu\text{s}$ to accelerate the maximum velocity in pure He while $0.25 \mu\text{s}$ when Ar is mixed into the He gas flow. In the Ar doped image, there are obvious bright spots in the tube, and the plasma is sufficiently accelerated to eject out of the tube at almost its maximum velocity. The initial acceleration of the bullet is due to the formation of an electron avalanche multiplication near the high-voltage electrode.⁷ When a small amount of Ar is introduced to the working gas, the electron avalanche multiplication is enhanced. On comparing the images at the beginning of the discharge phase, it is obvious that the discharge intensity in the pure He tube is lower than doping Ar working gas, as space electric field in the tube is lower, and the plasma is not fully accelerated.

To identify and compare the reactive species from the plasma jet during the mode transition, the OES in the wavelength range

from 300 to 800 nm is shown in Fig. 6(a) at Ar content of 0, 1, and 3 SLM. To compare the importance of the dominant species, the emission spectra are normalized to the maximum in Fig. 6(b). In Fig. 6(a), it can be found that the emission spectra are mainly dominated by OH(A), $\text{N}_2^+(\text{B})$, $\text{He}(3s^3\text{S})$, and $\text{O}(3p^5\text{P})$ emissions in pure He discharge. With the transition from pure He to pure Ar, $\text{N}_2^+(\text{B})$, $\text{He}(3s^3\text{S})$, and $\text{O}(3p^5\text{P})$ emissions are replaced by $\text{Ar}(4p \rightarrow 3s)$. As shown in Fig. 6(b), the emission spectrum of excited state $\text{O}(3p^5\text{P})$ and $\text{N}_2^+(\text{B})$ exhibits a low intensity in 1 SLM Ar and 3 SLM Ar emission spectrum. In pure He discharge, the intensity of OH is slightly lower than that of $\text{He}(3s^3\text{S})$, and $\text{N}_2^+(\text{B})$ and $\text{O}(3p^5\text{P})$ intensities can also account for 20% of $\text{He}(3s^3\text{S})$ intensity. As for Ar ($4p \rightarrow 3s$), the intensity of 3 SLM Ar is higher than 1 SLM Ar + 2 SLM He, which indicates a better argon ionization. The relationship of the relative emission intensity of the OH band is as follows: pure He < pure Ar < 1 SLM Ar + 2 SLM He.

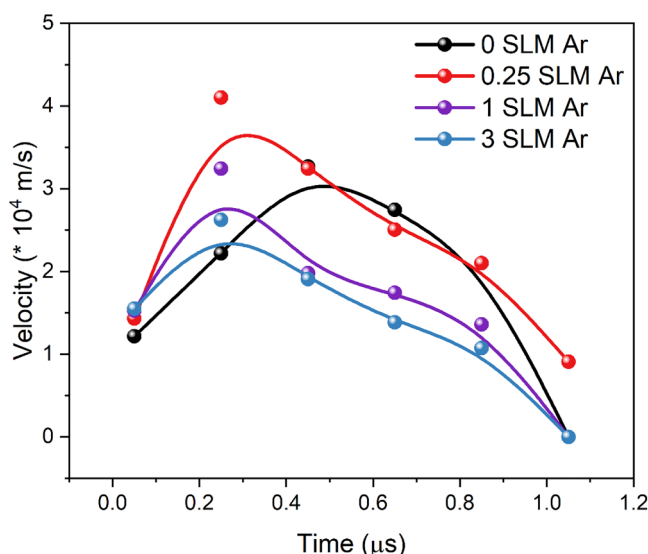


FIG. 5. Dependence of the velocity of the plasma jets bullets on discharge time under four working gases, 0 SLM Ar, 0.25 SLM Ar, 1 SLM Ar and 3 SLM Ar.

B. Regulation of aqueous RONS during discharge mode transition

To explore the variation relationship of RONS delivery into liquid during mode transition, the absorption spectra of PAW are employed. Figure 7 shows the absorption spectra and total absorbance of PAW after 2 and 5 min APPJ treatment under different Ar addition. In Figs. 7(a) and 7(b), the peak absorbance is highest at pure Ar, followed by pure He, and lowest at 1 SLM Ar. There is a significant distinction except for the peak values. The characteristic peak positions are between 200 and 220 nm at 5 min treatment and within 200 nm at 2 min except for 3 SLM Ar. The differences in peak profiles indicate the composition and concentration variation of RONS, as different species have different absorption cross sections. These differences correspond to the regime where NO_2^- , NO_3^- , or H_2O_2 is dominant.²⁵ RONS with relatively long estimated half-lives include (but not limited to) H_2O_2 , NO_2^- , and NO_3^- , and these are expected to be the main species contributing to the UV absorbance signal.²¹ The peak positions of PAW under 5 min treatment indicate a relatively high concentration ratio of NO_2^- and NO_3^- in PAW, while for 2 min treatment (except for 3 SLM Ar) the ratio of NO_2^- and NO_3^- is quite low.^{21,25} The relatively low ratio of NO_2^- and NO_3^- under 2 min is due to the absence of nitrogen or air in working gases, and the RNS could only come from the reactions with the ambient air. As for 3 SLM Ar under 2 min, pure Ar plasma could effectively interact with ambient air producing a significant influence of RNS. The analysis of RONS variation in PAW will be verified by the quantitative detection of H_2O_2 and NO_2^- . Figure 7(c) shows the total absorbance obtained by integration from Eq. (1). The total absorbance under 5 min treatment decreases from 4.4 to 2.0 between 0 and 1 SLM Ar admixture, then rises to 10.9 at 3 SLM Ar. This indicates that the activation effect of PAW

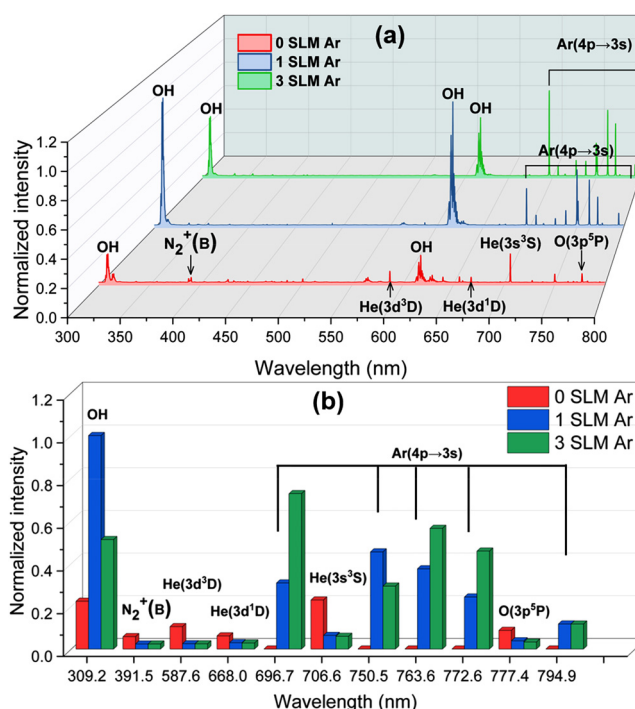


FIG. 6. (a) The emission spectra of plasma jet under three working gases, 0 SLM Ar (pure He), 1 SLM Ar and 3 SLM Ar (pure Ar). (b) The normalized intensity of the dominant active species. The measured point is located at the nozzle of the quartz tube.

exhibits the first decrease and then increase trend with the increase in Ar content.

The activation of de-ionized water not only generates abundant RONS but also changes the physicochemical properties. The pH and conductivity can affect the concentration and chemical activity of RONS²⁶ and finally affect the inactivation effect on cancer cells. The pH value and conductivity of PAW under 2 and 5 min treatment are shown in Fig. 8. In Fig. 8(a), there is a clear increase in the pH value with the addition of Ar that peaked at 1 SLM Ar admixture and the pH value under pure Ar discharge is lower than pure He. As for the conductivity, Fig. 8(b) shows that the conductivity of PAW first decreases and then increases with Ar addition, reaching the minimum value at 1 SLM Ar. This result is consistent with the result of pH and total absorbance. It can also be found that the PAW for 5 min has a lower pH value and higher conductivity than that for 2 min at the same Ar content. Electrical conductivity is related to the concentration of reactive ions existing in the liquid.²⁷ The formation of RNS during PAW generation will contribute to the increase in the conductivity of PAW.²⁸ Electrical conductivity has been reported to be directly connected to pH, demonstrating an inverse correlation.²⁹ The pH value can reflect the concentration of H^+ in the solution, and H^+ mainly comes from the ionization of long-lived species produced by plasma gas species entering the liquid phase, such as HNO_3 , HNO_2 , and

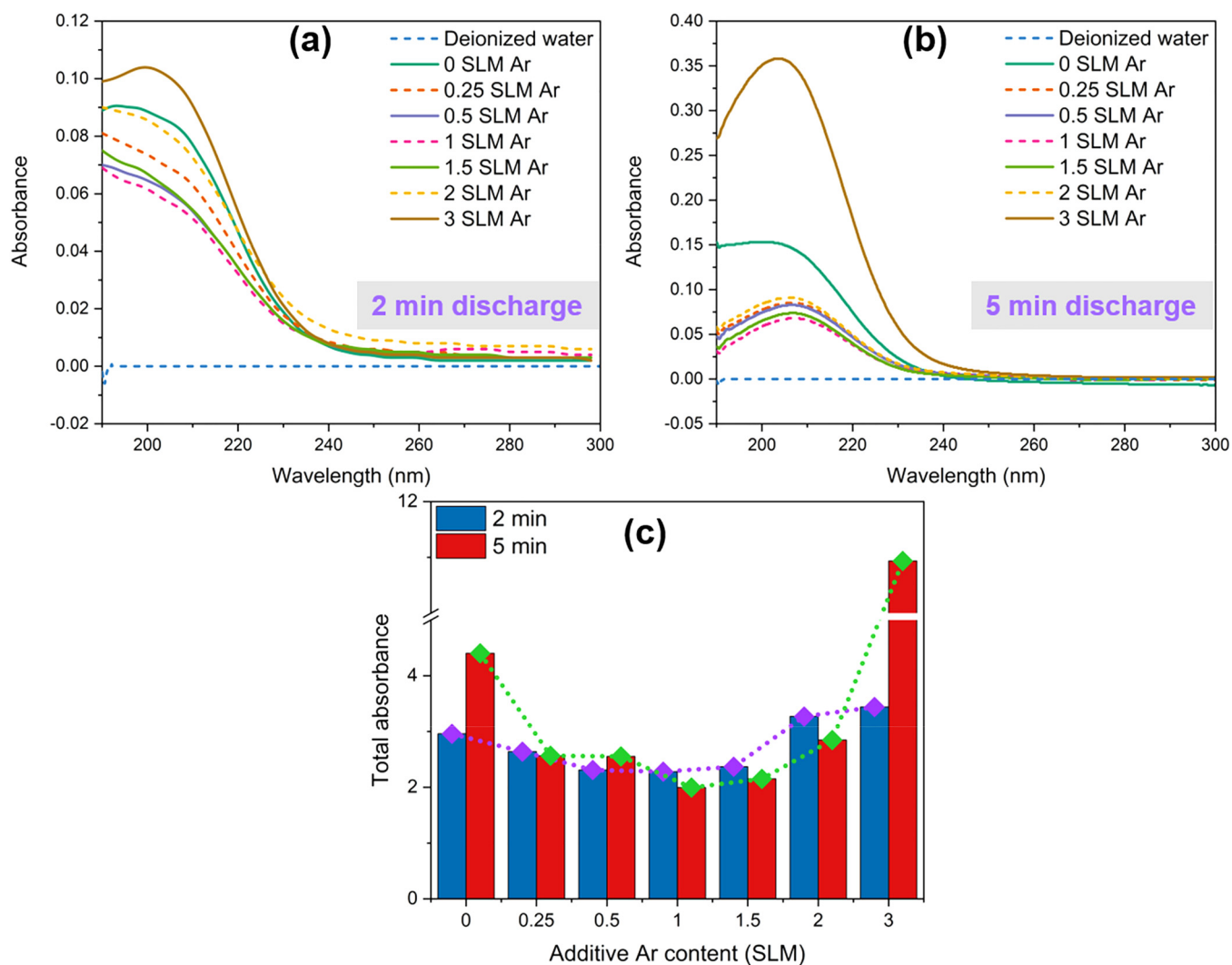
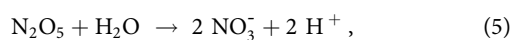
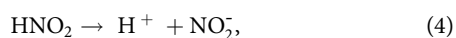
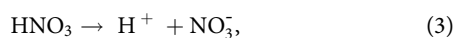


FIG. 7. Absorption spectra profiles of PAW under (a) 2 min and (b) 5 min APPJ treatment during discharge mode transition. (c) Total absorbance of PAW during discharge mode transition. 0 SLM Ar represents pure He and 3 SLM Ar represents pure Ar.

H_2O_2 .^{30,31} The equations are as follows:



It can be seen from the equations that $[\text{H}^+] \approx [\text{NO}_3^-] + [\text{NO}_2^-]$. So the concentration of RONS is shown in the following paragraph.

To clarify how mode transition influences aqueous RONS in PAW, the concentrations of H_2O_2 , NO_2^- , and TEMPONE are measured and shown in Fig. 9. In Figs. 9(a) and 9(b), it is found that both NO_2^- and H_2O_2 concentrations after treatment for 5 min show a trend of the first decrease and then increase, which is consistent with the previous results of the absorption spectrum, pH, and electrical conductivity. It is again confirmed that the concentration of long-lived RONS would decrease first when a small amount of Ar is mixed in He. The concentrations of NO_2^- and H_2O_2 generated by Ar discharge are higher than He discharge. Therefore, as the additive Ar content continues to increase, the discharge mode will finally change to pure Ar discharge, and the concentration of RONS in PAW shows an upward trend. According to the long-lived RONS (H_2O_2 and NO_2^-) concentration and previous

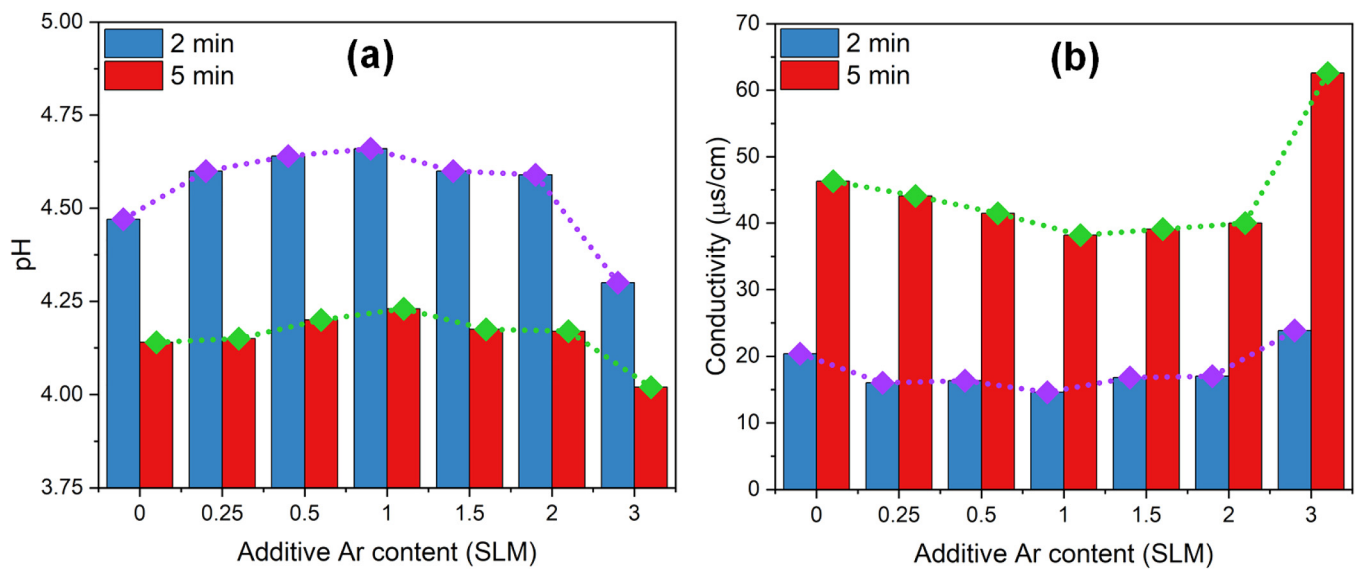


FIG. 8. The effects of (a) pH value and (b) conductivity of PAW on the different Ar addition under 2 min and 5 min treatment. 0 SLM Ar represents pure He and 3 SLM Ar represents pure Ar.

research results, the doping ratio of jet mode conversion can be speculated at around 1 SLM Ar. The possible explanation for this first decrease and then increase trend of H_2O_2 and NO_2^- is as follows. The energy of the excited He species (19.8 eV) exceeds the first ionization energy of almost all other gas atoms or molecules. Due to the high energies of these reactive He species, additive Ar in the working gas and the surrounding air will be ionized by penning and charge exchange processes or be otherwise collisionally excited.³² Penning ionization of ground-state Ar was the dominant quenching pathway for metastable He, and the Penning ionization of N_2 and O_2 was weakened which resulting in the reduction of NO_2^- and H_2O_2 . However, with the further increase in Ar,

metastable He was effectively quenched out. But the density of excited Ar species in the plume increases, due to direct formation via electron impact excitation and cascade from higher excited levels in the active discharge.³² The Penning ionization of N_2 and O_2 was enhanced, which increases NO_2^- and H_2O_2 . Therefore, the turning point occurred when the penning ionization of Ar was high and the direct ionization of Ar was not enough.

The concentration of TEMPONE is shown in Fig. 9(c), and the concentration of TEMPONE represents the total concentration of both O_2^- and $\text{ONOO}^-/\text{ONOOH}$. With the increase in Ar doping proportion, the concentration of short-lived O_2^- and $\text{ONOO}^-/\text{ONOOH}$ generally presents a rising trend, but the amplitude of the

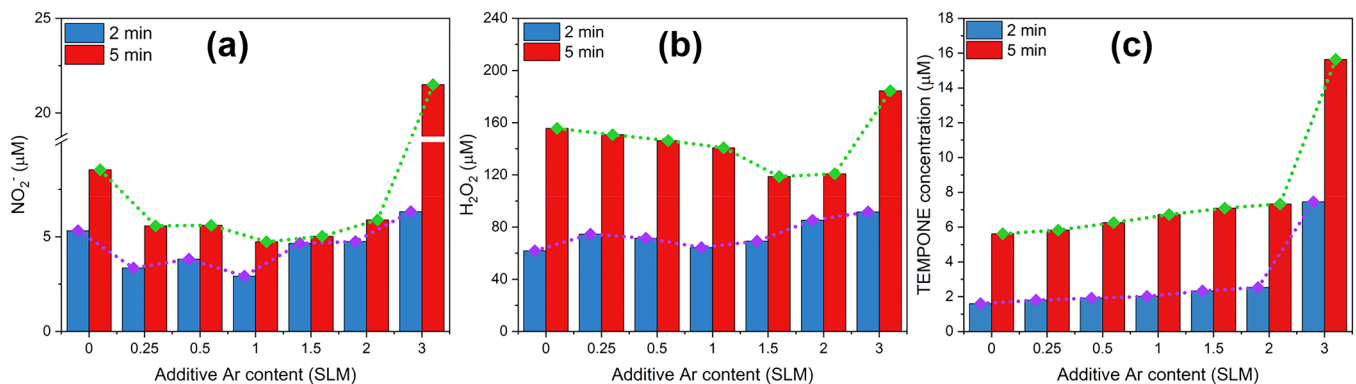
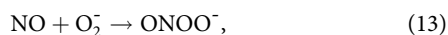
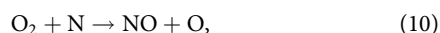
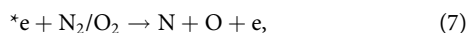


FIG. 9. The effects of the concentration of (a) NO_2^- , (b) H_2O_2 , and (c) TEMPONE in PAW on the different Ar addition under 2 min and 5 min APPJ treatment. 0 SLM Ar represents pure He and 3 SLM Ar represents pure Ar.

rise is limited when He still exists. Under the pure Ar plasma jet, the concentration of short-lived species increases sharply. So it can be inferred that the filamentous discharge mode is more favorable to the generation of short-lived species.^{13,23} This result may be explained by the filament channels. Compared with homogeneous discharge, the filament channels with high electron density under filaments discharge were converted by electron avalanches. As the Ar content increases, the working gas changes from pure He to pure Ar gradually, the discharge channel forms, and the electron density increases. On the one hand, the electron in the channel reacts with N_2 and O_2 in the open air and generates NO through a series of chemical reactions. NO further reacts at the gas-liquid surface to generate $ONOO^-/ONOOH$. These could be explained by reactions (7)–(14). On the other hand, O_2^- can be produced by the deprotonation of the hydroperoxyl radical OOH, which can be generated from the reactions of molecular oxygen with highly energetic electrons,^{27,33}



C. The inactivation effect against tumor cells during discharge mode transition

To further investigate the inactivation effect against tumor cells *in vitro* during the mode transformation, Fig. 10 shows the cell viability of A549 lung cancer cells and the corresponding result. Compared to the cells in the control (Con) group, it is obvious that the number of living cells with PAW treatment is reduced due to the abundant RONS, where H_2O_2 can induce apoptosis and necrosis, and NO_2^- can cause cell death through DNA double-strand break.³⁴ The DI group is the cancer cell that survived after de-ionized water treatment for 24 h culture, excluding the effect of low osmotic pressure that shows the limited effect on viability in this situation. With the increase in the additive content of Ar, the corresponding relative cell activity shows an upward and then downward trend and the maximum value corresponds to 1 SLM Ar addition. Cell death is mainly represented as necrosis and apoptosis. To quantitatively describe the state of cell death, the results extracted from the ratio of cell apoptosis by flow cytometry with FITC and PI staining kit are presented in Fig. 11. The late apoptotic cells are shown in the upper right quadrant, the early

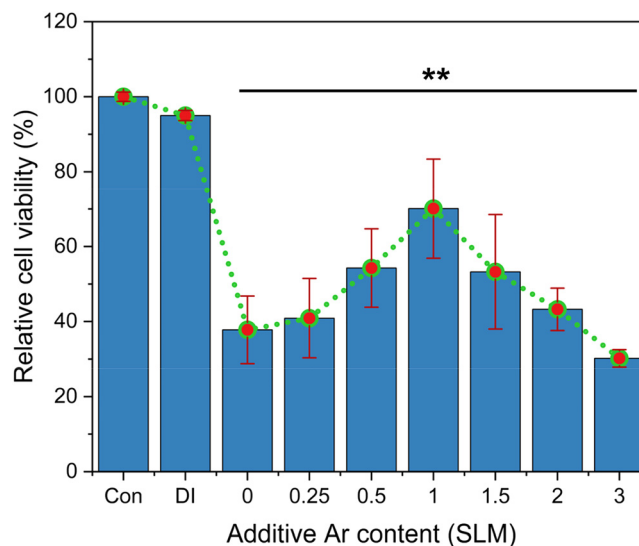


FIG. 10. The cell viability of A549 treated by PAW during discharge mode transition under 5 min APPJ treatment. The cells were cultured under 50% RPMP1640 + 50% PAW treatment for 24 h.

apoptotic cells are shown in the lower right quadrant, the upper left quadrant mainly represents necrosis cells, and the lower left quadrant represents living cells. The apoptosis rate of A549 cells is obtained by the sum of early and late apoptosis. The final result is shown in Fig. 12. It can be seen that the rate of apoptosis and cell activity is inversely proportional, the higher the viability, the less the proportion of apoptotic cells. The lowest apoptosis rate of 14.8% is observed with the addition of 1 SLM Ar. The apoptosis rate is 30.7% for pure He plasma treatment and 45.7% for pure Ar plasma treatment, indicating that pure Ar jet has a better inactivation effect than pure He jet. The cell necrosis rate during the plasma jets transformation is less than 1.2%, indicating a good cancer-killing effect without hurting healthy cells. To display the inactivation effects of these plasma jets visually, the microscopic image of A549 cancer cells is shown in Fig. 13. The red spot indicates dead cancer cells while the bright spot is intact cell membranes indicating living cells. Compared with the control and DI group, it can be concluded that the number of living cells remaining after treatment with pure Ar plasma is less, followed by pure He. The PAW under 1 SLM Ar treatment results in the most living cells in fluorescent images in the experimental group. In our case, the cell viability has a positive correlation with concentrations of H_2O_2 , NO_2^- , and $ONOO^-/ONOOH$, implying that $ONOO^-/ONOOH$ might be responsible for the cell inactivation. Especially under the filamentous mode of the Ar plasma jet, the high productions of key species NO_2^- , H_2O_2 , and $ONOO^-/ONOOH$ would be obtained. It is well accepted that $ONOO^-/ONOOH$ has significant cytotoxicity and can react with the cell walls to result in breaking biological structures and then access the inside cell to damage amino acids and nucleic acids, finally disrupt the function of the organelle.^{35,36} It should be mentioned that the cancer cell killing

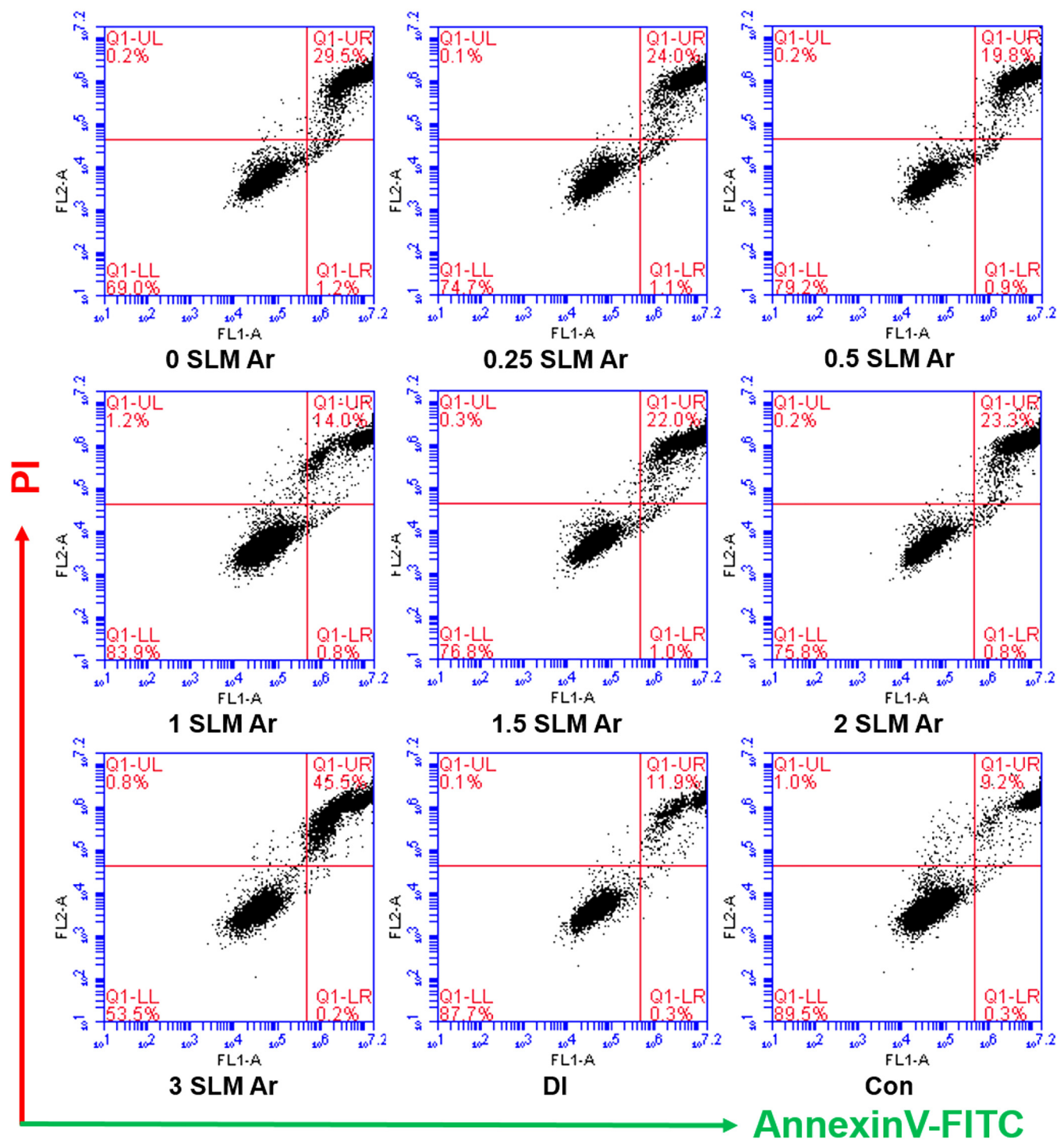


FIG. 11. The apoptosis state of A549 cells induced by PAW during discharge mode transition under 5 min APPJ treatment. The cells were cultured under 50% RPMP1640 + 50% PAW treatment for 24 h.

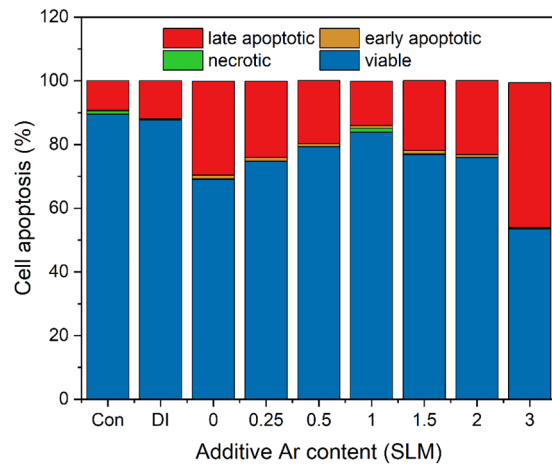


FIG. 12. The flow cytometry analysis of each apoptotic stage of A549 cells induced by PAW corresponding to Fig. 11.

effect of H_2O_2 is synergistically enhanced by NO_2^- , because H_2O_2 and NO_2^- can continuously produce $\text{ONOO}^-/\text{ONOOH}$ in the mixed solution through reactions (15) and (16).^{27,31} Additionally, H_2O_2 and NO_2^- are also contributing to the selectivity of the antitumor effect due to their high oxidation ability and long lifetime from the plasma-induced liquid,^{30,35}



IV. CONCLUSION

In this study, we investigated the mode transformation process of plasma jet mode from diffuse to filamentous discharge and the corresponding activation effect by adjusting different Ar contents in working gas. It is found that the discharge power first decreases and then increases with Ar addition, and the minimum power is located at 1 SLM Ar. The color and length of the plasma jet also

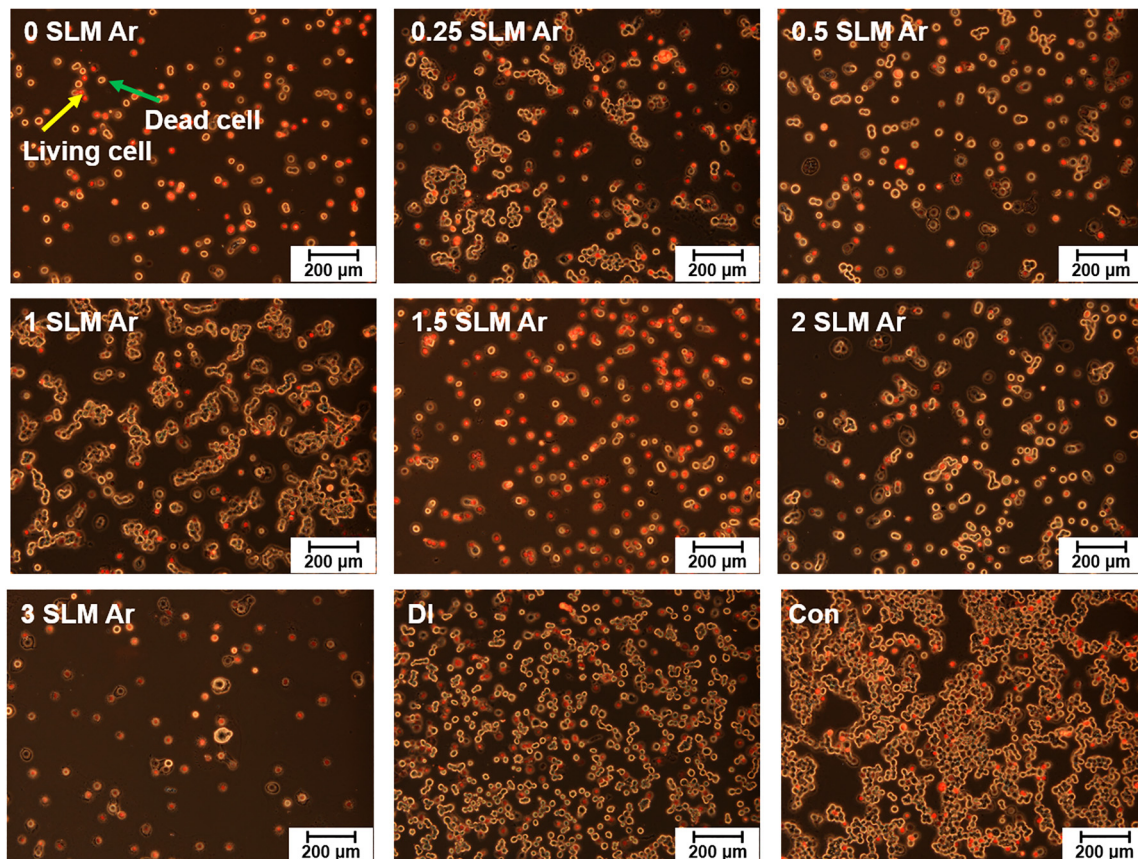


FIG. 13. Fluorescent images of apoptotic cells captured in the same condition of Fig. 11, the red pot indicates the dead cell, the bright pot indicates living cell.

transform from the macroscopic view. From the microcosmic view, ICCD images show that the plasma bullets gradually change from droplet shape to spindle shape with the doping of Ar, and the time for the plasma to reach the maximum velocity is reduced from 0.45 to 0.25 μ s. The emission lines of $N_2^+(B)$, $He(3s^3S)$, and $O(3p^5P)$ are observed in pure He plasma jet, while the lines of $He(3s^3S)$ almost disappear under the condition of 1 SLM Ar. It is verified that the characteristic of the He plasma jet disappears and is replaced by a discharge closer to Ar plasma. For liquid chemistry of PAW induced by plasma jet, it is found that the conductivity first decreases and then increases with the Ar doping ratio, while the pH first increases and then decreases. The concentration of H_2O_2 and NO_2^- in PAW also decreases first and then increases with the Ar doping ratio. The concentration of O_2^- and $ONOO^-/ONOOH$ increased with the addition of Ar. It can be inferred that the filamentous discharge mode is more favorable to the generation of short-lived species. The PAW induced by the Ar plasma jet has a remarkable effect against tumor cells *in vitro*, which may be due to the high production of key species NO_2^- , H_2O_2 , and $ONOO^-/ONOOH$ produced under filamentous mode.

ACKNOWLEDGMENTS

This study was financially supported by the National Natural Science Foundation of China (NNSFC) (Grant Nos. 12075188, 51707150, and 51837008), Special Fund of China Postdoctoral Science Foundation (Grant No. 2021T140536), and China Postdoctoral Science Foundation (Grant No. 2021M692529).

DATA AVAILABILITY

The data that support the findings of this study are available from the corresponding authors upon reasonable request.

REFERENCES

- ¹J. Hong, A. Murphy, B. Ashford, P. Cullen, T. Belmonte, and K. Ostrikov, *Rev. Mod. Phys.* **4**, 1 (2020).
- ²F. Sohbatzadeh, M. Eshghabadi, and T. Mohsenpour, *Nanotechnology* **29**, 265603 (2018).
- ³F. Rezaei, Y. Gorbanev, M. Chys, A. Nikiforov, S. W. Van Hulle, P. Cos, A. Bogaerts, and N. De Geyter, *Plasma Process. Polym.* **15**, 1700226 (2018).
- ⁴K. N. Pandiyaraj, D. Vasu, P. Padmanabhan, R. Ghobeira, P. S. E. Tabaei, P. Cools, N. De Geyter, R. Morent, R. Deshmukh, and M. Pichumani, *Surf. Coat. Technol.* **389**, 125642 (2020).
- ⁵F. G. C. Ekezie, J. H. Cheng, and D. W. Sun, *Food Chem.* **276**, 147 (2019).
- ⁶S. Choi, P. Attri, I. Lee, J. Oh, J.-H. Yun, J. H. Park, E. H. Choi, and W. Lee, *Sci. Rep.* **7**, 1 (2017).
- ⁷Z. J. Liu, W. Wang, D. X. Liu, C. X. Zhou, T. T. He, W. J. Xia, and M. G. Kong, *Phys. Plasmas* **26**, 053507 (2019).
- ⁸X. J. Shao, N. Jiang, G. J. Zhang, and Z. X. Cao, *Appl. Phys. Lett.* **101**, 253509 (2012).
- ⁹Y. Xian, X. Lu, Z. Tang, Q. Xiong, W. Gong, D. Liu, Z. Jiang, and Y. Pan, *J. Phys. D: Appl. Phys.* **107**, 063308 (2010).
- ¹⁰Y. Du, G. Nayak, G. Oinuma, Z. Peng, and P. J. Bruggeman, *J. Phys. D: Appl. Phys.* **50**, 145201 (2017).
- ¹¹S. Takamura, S. Amano, T. Kurata, H. Kasada, J. Yamamoto, M. A. Razzak, G. Kushida, N. Ohno, and M. Kando, *J. Phys. D: Appl. Phys.* **110**, 043301 (2011).
- ¹²Z. J. Liu, C. X. Zhou, D. X. Liu, D. H. Xu, W. J. Xia, Q. J. Cui, B. C. Wang, and M. G. Kong, *Phys. Plasmas* **25**, 013528 (2018).
- ¹³T. Shao, C. Zhang, R. X. Wang, Y. X. Zhou, Q. Xie, and Z. Fang, *IEEE Trans. Plasma Sci.* **43**, 726 (2015).
- ¹⁴Z. S. Chang, N. Jiang, G. J. Zhang, and Z. X. Cao, *J. Phys. D: Appl. Phys.* **115**, 103301 (2014).
- ¹⁵Q. Li, W. C. Zhu, X. M. Zhu, and Y. K. Pu, *J. Phys. D: Appl. Phys.* **43**, 382001 (2010).
- ¹⁶H. Y. Luo, Z. Liang, B. Lv, X. X. Wang, Z. C. Guan, and L. M. Wang, *Appl. Phys. Lett.* **91**, 221504 (2007).
- ¹⁷S. Hofmann, A. Van Gessel, T. Verreycken, and P. Bruggeman, *Plasma Sources Sci. Technol.* **20**, 065010 (2011).
- ¹⁸S. Wang, V. Schulz-Von der Gathen, and H. F. Döbele, *Appl. Phys. Lett.* **83**, 3272 (2003).
- ¹⁹Z. Q. Chen, B. K. Zhou, H. Zhang, L. L. Hong, C. L. Zou, P. Li, W. D. Zhao, X. D. Liu, O. Stepanova, and A. Kudryavtsev, *Chin. Phys. B* **27**, 055202 (2018).
- ²⁰K. Ogawa, J. S. Oh, N. Gaur, S. H. Hong, H. Kurita, A. Mizuno, A. Hatta, R. D. Short, M. Ito, and E. J. Szili, *Jpn. J. Appl. Phys.* **58**, SAAB01 (2018).
- ²¹E. J. Szili, J. S. Oh, S. H. Hong, A. Hatta, and R. D. Short, *J. Phys. D: Appl. Phys.* **48**, 202001 (2015).
- ²²D. B. Nguyen, Q. H. Trinh, W. G. Lee, and Y. S. Mok, *Plasma Sci. Technol.* **21**, 095401 (2019).
- ²³H. Y. Lee, J. H. Choi, J. W. Hong, G. C. Kim, and H. J. Lee, *J. Phys. D: Appl. Phys.* **51**, 215401 (2018).
- ²⁴R. J. Leiweke, B. L. Sands, and B. N. Ganguly, *IEEE Trans. Plasma Sci.* **39**, 2304 (2011).
- ²⁵T. Moiseev, N. Misra, S. Patil, P. Cullen, P. Bourke, K. Keener, and J. Mosnier, *Plasma Sources Sci. Technol.* **23**, 065033 (2014).
- ²⁶Z. C. Liu, D. X. Liu, S. T. Luo, W. T. Wang, Z. J. Liu, A. J. Yang, M. Z. Rong, H. L. Chen, and M. G. Kong, *J. Phys. D: Appl. Phys.* **52**, 415201 (2019).
- ²⁷R. W. Zhou, R. S. Zhou, P. Y. Wang, Y. b. Xian, A. Mai Prochnow, X. P. Lu, P. J. Cullen, K. Ostrikov, and K. Bazaka, *J. Phys. D: Appl. Phys.* **53**, 303001 (2020).
- ²⁸I.-E. Vlad and S. D. Anghel, *J. Electrostat.* **87**, 284 (2017).
- ²⁹Y. M. Zhao, A. Patange, D. W. Sun, and B. Tiwari, *Compr. Rev. Food Sci. Food Saf.* **19**, 3951 (2020).
- ³⁰P. Lukes, E. Dolezalova, I. Sisrova, and M. Clupek, *Plasma Sources Sci. Technol.* **23**, 015019 (2014).
- ³¹Z. J. Liu, S. T. Wang, B. L. Pang, H. Y. Zhang, Y. T. Gao, D. H. Xu, and M. G. Kong, *J. Phys. D: Appl. Phys.* **54**, 215203 (2021).
- ³²B. L. Sands, R. J. Leiweke, and B. N. Ganguly, *J. Phys. D: Appl. Phys.* **43**, 282001 (2010).
- ³³Z. J. Liu, D. H. Xu, D. X. Liu, Q. J. Cui, H. F. Cai, Q. S. Li, H. L. Chen, and M. G. Kong, *J. Phys. D: Appl. Phys.* **50**, 195204 (2017).
- ³⁴Z. T. Chen, X. Q. Cheng, L. Lin, and M. Keidar, *J. Phys. D: Appl. Phys.* **50**, 015208 (2016).
- ³⁵Z. J. Liu, D. H. Xu, C. X. Zhou, Q. J. Cui, T. T. He, Z. Y. Chen, D. X. Liu, H. L. Chen, and M. G. Kong, *Plasma Chem. Plasma Process.* **38**, 953 (2018).
- ³⁶R. W. Zhou, R. S. Zhou, K. Prasad, Z. Fang, R. Speight, K. Bazaka, and K. Ostrikov, *Green Chem.* **20**, 5276 (2018).